ADVANCED HEALTHCARE MATERIALS

Supporting Information

for *Adv. Healthcare Mater.,* DOI: 10.1002/adhm.201300610

Characterization of Conjugated Polymer Actuation under Cerebral Physiological Conditions

*Eugene Dariush Daneshvar and Elisabeth Smela**

Supporting Information

for

Characterization of Conjugated Polymer Actuation Under Cerebral Physiological Conditions

by

Eugene Dariush Daneshvar and Elisabeth Smela

S1. Variation among samples

In order to explore the extent of sample-to-sample variation under nominally identical electro-deposition and cycling conditions, six samples (the ones in Section **Error! Reference source not found.** that were subsequently cycled at room temperature) that had been polymerized one at a time on the same day were compared with six samples (the ones in Section **Error! Reference source not found.** that were later cycled at 37 °C) that had been polymerized simultaneously on another day. The same current density was used in all cases (1 mA/cm^2).

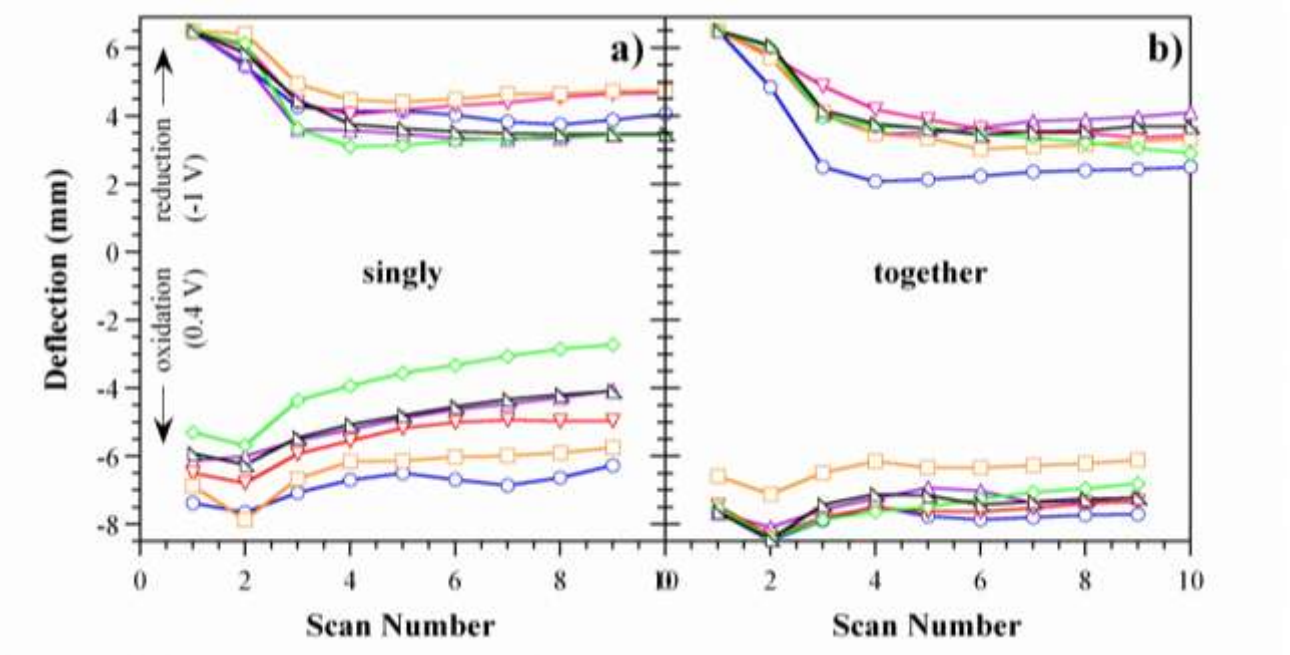

Sup. Figure 1. Maximum deflection during oxidation and reduction in NaDBS at 22 °C as a function of cycle number. a) Six bilayers on which the PPy(DBS) was polymerized separately (one bilayer at a time). b) Six bilayers on which the PPy(DBS) was polymerized simultaneously.

Sup. Figure 1 shows the variation in maximum deflections for both sets of samples during the first 10 cycles in room temperature NaDBS. The initial deflections in the reduced state varied, with an average of 6.5 mm and a standard deviation of 0.6 mm. In order to facilitate comparison, all the

deflection data in Sup. Figure 1 were shifted so that the starting reduction position was the same, 6.5 mm.

The (shifted) average deflection during reduction in scan 10 was 4.0 mm $\pm$ 0.6 mm for the films deposited separately and 3.3 mm $\pm$ 0.6 mm for the PPy deposited simultaneously. The second set drifted somewhat further from the starting position, on average. The *variation* in the final reduced positions was the same $\pm$0.6 mm for all twelve beams, however.

During oxidation the bilayers made together deflected more than those made individually and showed less variation in the oxidized-state starting positions: in scan 1 the average was -6.3 mm$\pm$ 0.7 mm, compared with -7.4 mm $\pm$ 0.4 mm for the bilayers made together. The variation among bilayer tip positions increased by cycling: at scan 9, the average was -4.6 mm $\pm$ 1.3 mm for the individually-polymerized beams and for the beams polymerized together it was -7.1 mm $\pm$ 0.6 mm.

These data indicate that there are differences among beams made on the same day, even if they are all made together, and that there is even greater variation if they are made one at a time. Nevertheless, the behavior was broadly similar for all the bilayers, showing a decrease in deflection within the first 4 cycles in both the PPy-side-out and PPy-side-in directions but stabilizing thereafter.

S2. Deflection of all twelve bilayers under all four conditions

The deflections of all the bilayers are shown in Sup. Figure 2. The samples used in the main text, **Error! Reference source not found.**, were: NaDBS, 22 °C: ▼ (sample 2), aCSF, 22 °C: ▼ (sample 2), NaDBS, 37 °C: ▼ (sample 2), aCSF, 37 °C: ▲ (sample 3).

Sup. Table 1. Peak to peak deflections for the samples in Error! Reference source not found. **of the main text.**

	Peak-to-Peak Deflection (mm)			
	NaDBS RT	NaDBS 37 °C	aCSF RT	aCSF 37 °C
Scan 9	9.61	10.70	7.56	9.84
Scan 19	10.03	13.27	6.80	12.26
	Deflection Difference from Scan 19 to 9 (mm)			
Scan 19-9	0.42	2.56	-0.76	2.42
	Peak-to-Peak Deflection Ratio (Scan 19/9)			
Scan 19/9	1.04	1.24	0.90	1.25

As shown in **Error! Reference source not found.** of the main text, during each CV scan the bilayer beam would deflect to a proximal position relative to the straight position during reduction and oxidation. Sup. Table 1 shows the net deflections in scans 9 and 19 for the samples shown in **Error!**

Reference source not found. of the main text. In addition, the differences in displacements between scans 19 and 9 as well as their ratios are also given.

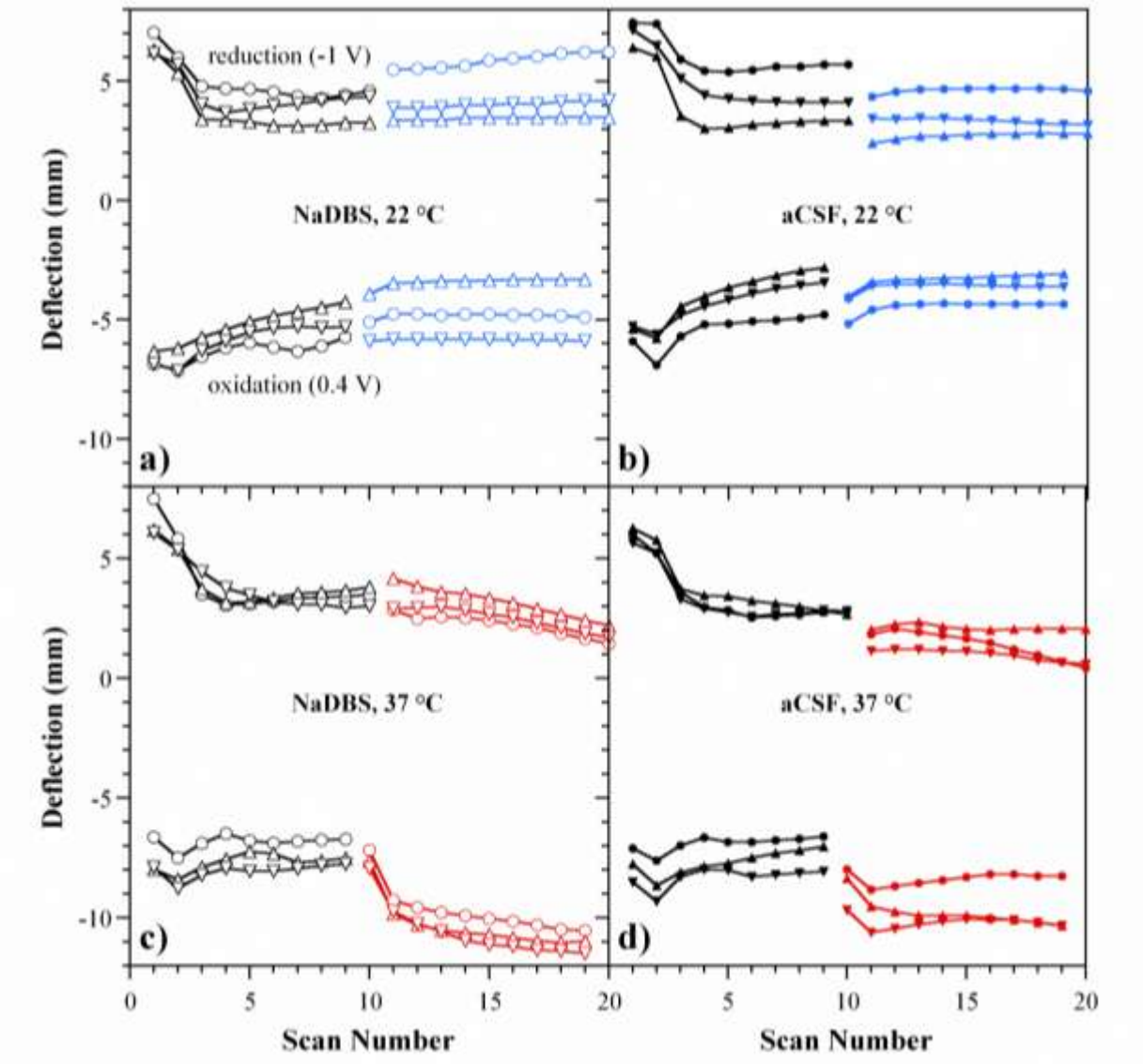

Sup. Figure 2. The maximum deflections during cyclic voltammetry of all twelve samples, cycled in NaDBS at 22 °C for the first 10 cycles, then in the medium and at the temperature indicated. (For correlation with Sup. Figure 3-Sup. Figure 6, circles = sample 1, up-pointing triangles = sample 2, and down-pointing triangles = sample 3.)

S3. Cyclic voltammetry of bilayers under the four conditions

Error! Reference source not found. of the main text shows current-voltage relationships of representative samples in each of the four solutions. To illustrate the variability, the cyclic voltammograms (CVs) of all three samples in each of the four solutions are shown in Sup. Figure 3-

Sup. Figure 6. PPy(DBS) was galvanostatically (constant current) polymerized to a thickness of 11.3 ± 0.8 μm. The scan rate was 10 mV/s, and the reference electrode was Ag/AgCl.

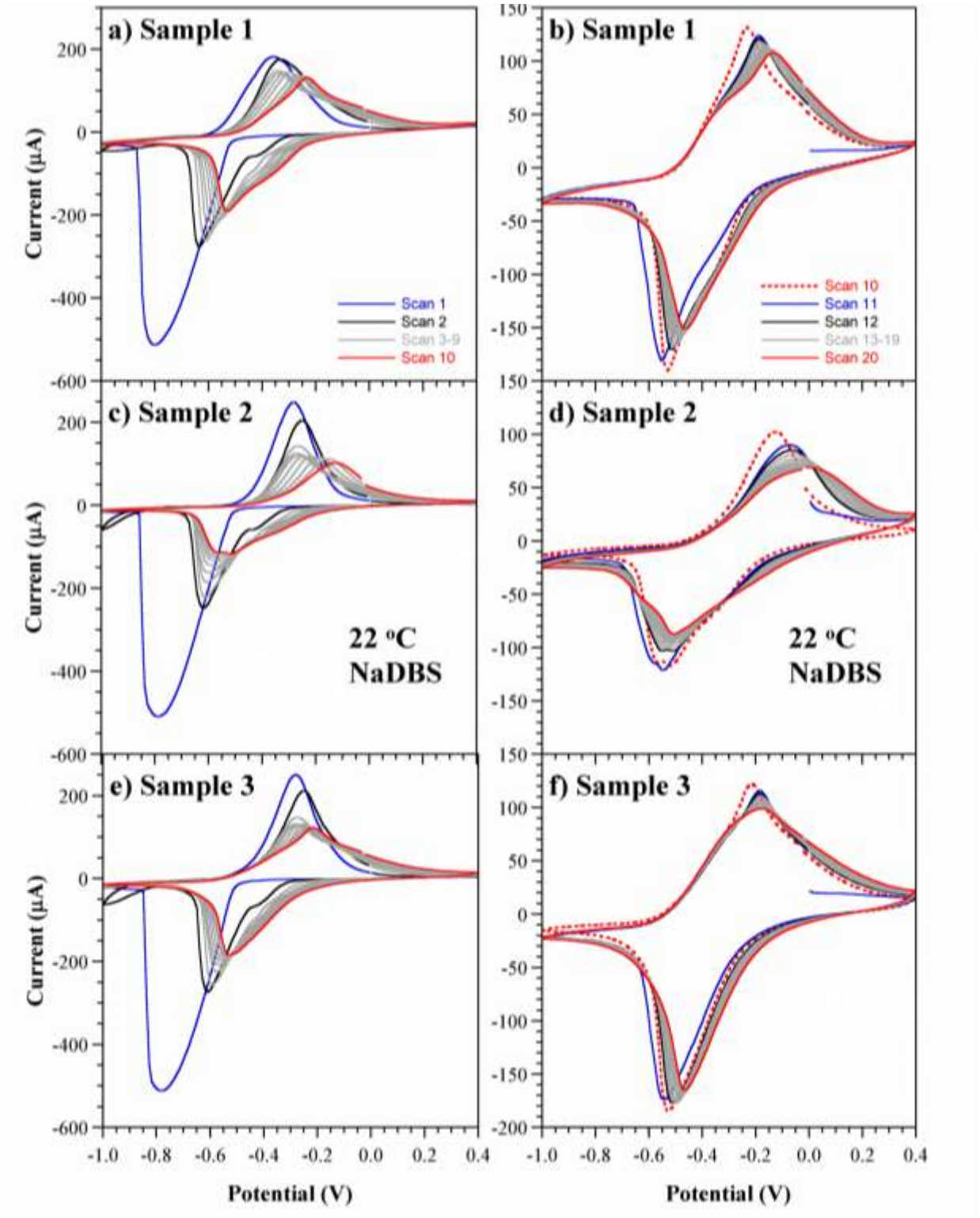

Sup. Figure 3. Cyclic voltammograms of three samples cycled in NaDBS at 22 °C for (left) the first 10 scans and then (right) the second 10 scans. To facilitate comparison, since the scales on the left and the right differ, scan 10 is repeated. Sample 3 was used in the main text.

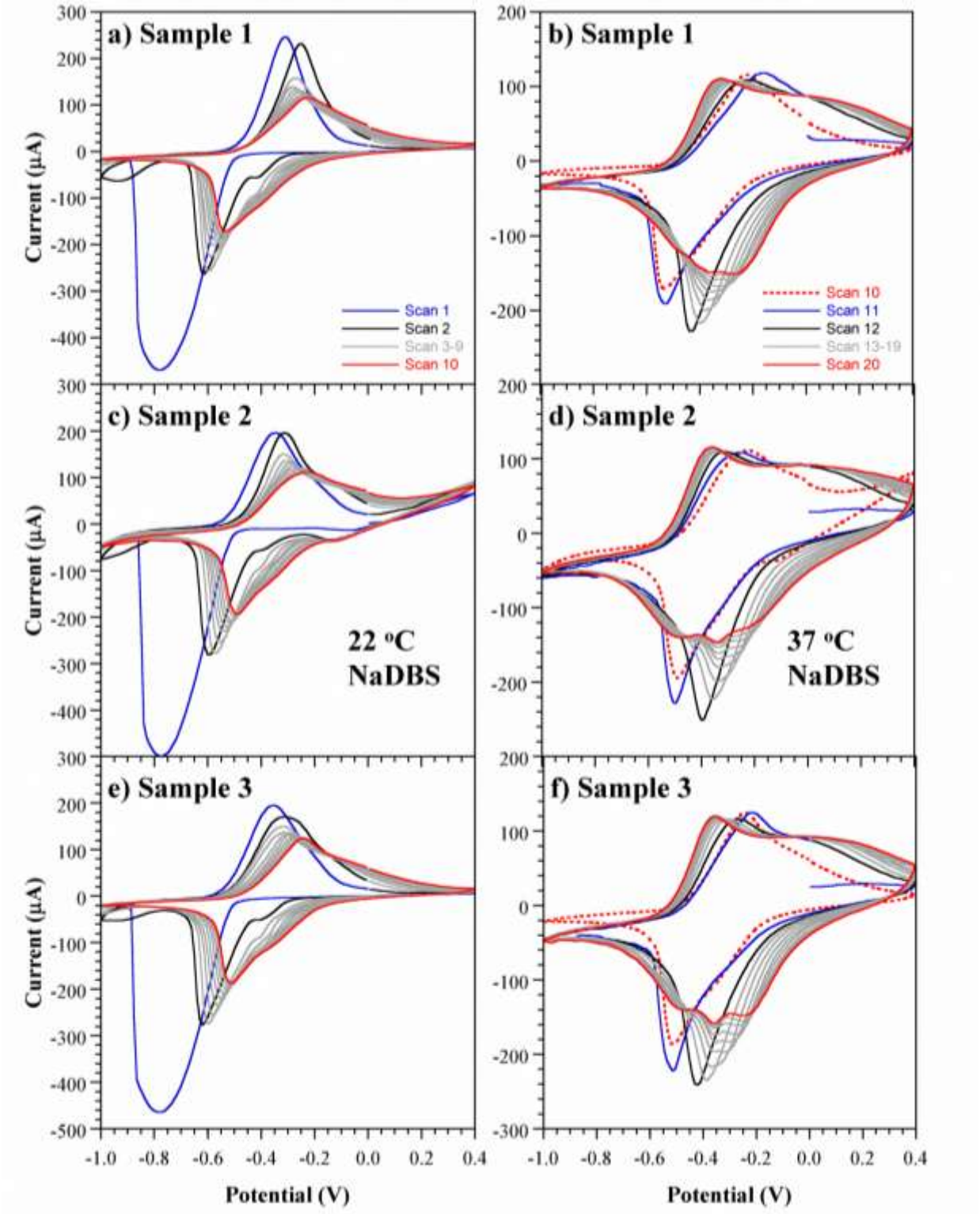

Sup. Figure 4. Cyclic voltammograms of three samples cycled in NaDBS at (left) 22 °C for the first 10 scans and then (right) at 37 °C for the second 10 scans. Sample 2 was used in the main text.

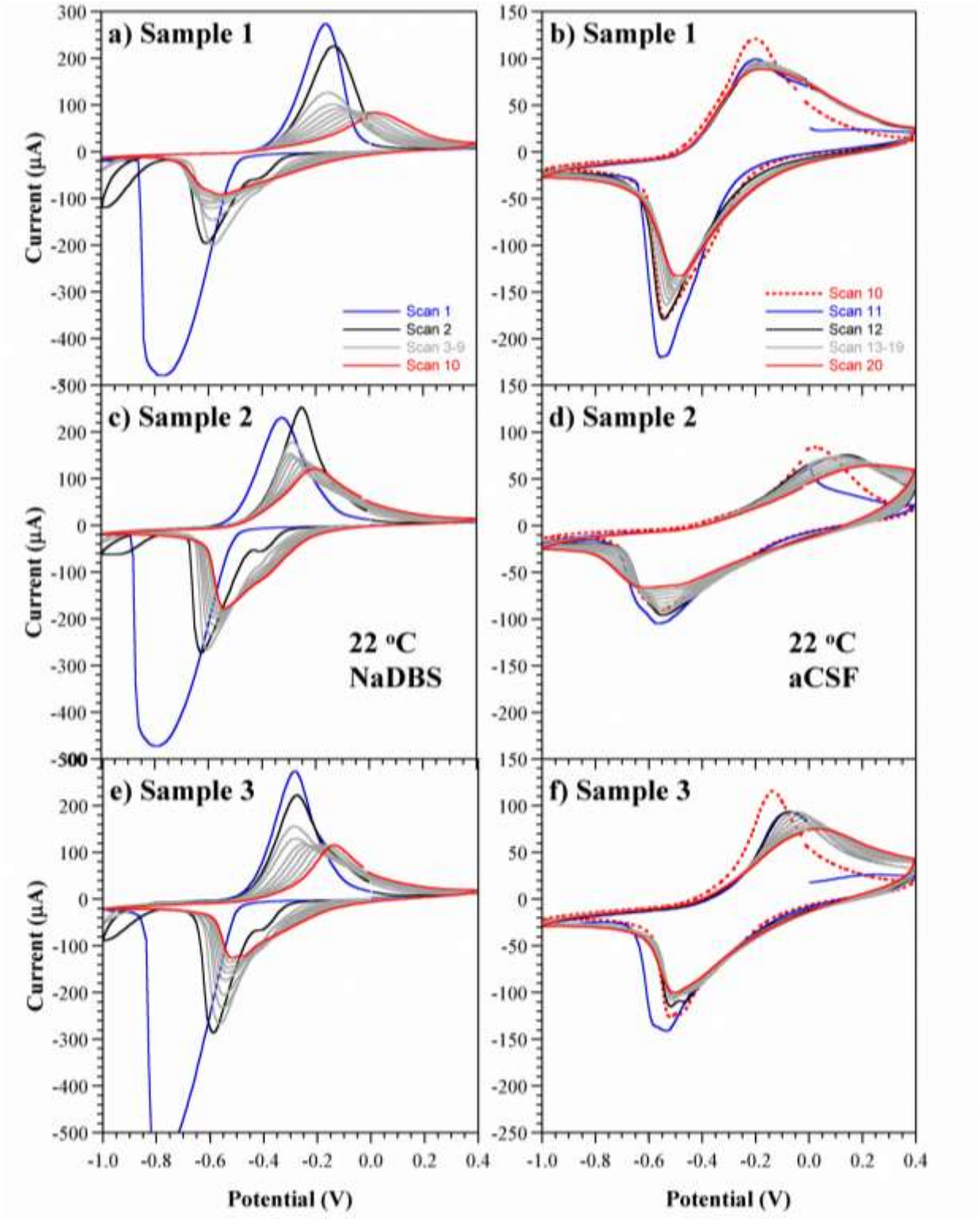

Sup. Figure 5. Cyclic voltammograms of three samples cycled (left) in NaDBS at 22 °C for the first 10 scans and then (right) in aCSF at 22 °C for the second 10 scans. Sample 3 was used in the main text.

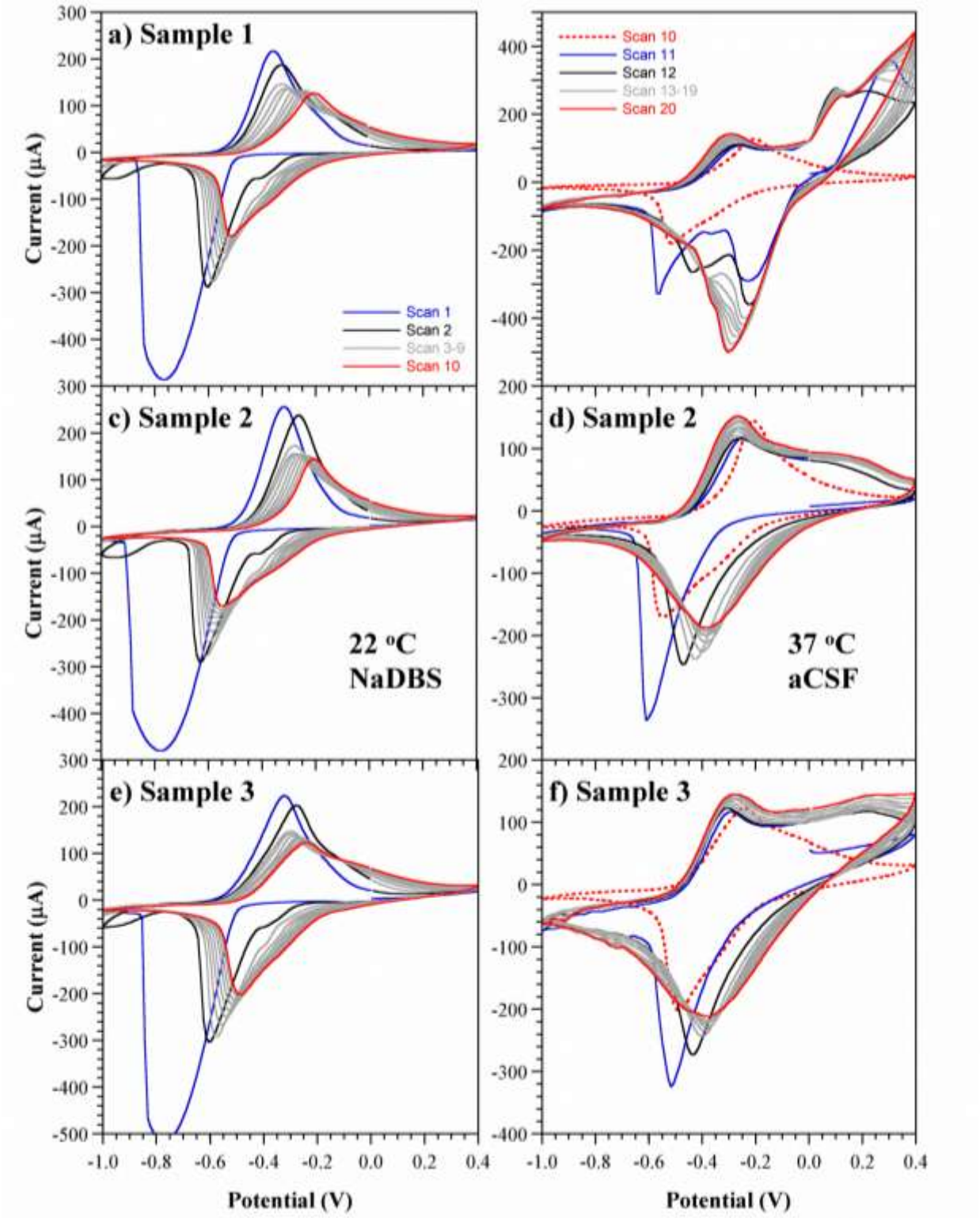

Sup. Figure 6. Cyclic voltammograms of three samples cycled (left) in NaDBS at 22 °C for the first 10 scans and then (right) in aCSF at 37 °C for the second 10 scans. Note that the vertical scale for (b) is almost twice that for (d) and (f). Sample 2 was used in the main text.

The expected large current is seen during the very first reduction scan in NaDBS [61]. Thereafter, the reduction peak shifts anodically (to the right) and decreases in height. The second scan shows a small current at -1 V that is not seen in any of the other scans. The oxidation peak shifts anodically and also decreases in size with scan number. The CVs have not completely stabilized after the first 10 scans. In Sup. Figure 3, the cycling continues in the same NaDBS solution, after the samples were removed from the cell and placed back into it. The anodic shifts and reductions in current magnitude continue. It is possible that an irreversible change is occurring, such as delamination. Sample 3 in Sup. Figure 3f is an exception, since the CVs more or less stabilize; this sample also has the highest currents, or exchanged charge, supporting the hypothesis that the others may be delaminating.

As noted above, the samples later cycled at room temperature (Sup. Figure 3 and Sup. Figure 5) were polymerized individually, while those later cycled at 37 °C (Sup. Figure 4 and Sup. Figure 6) were all polymerized together. The CVs of the former showed somewhat greater variability upon cycling in NaDBS than did the latter, but the basic behavior was the same.

Sup. Figure 7 overlays the current-voltage relationships in the four solutions in scan 19 for the samples of **Error! Reference source not found.** in the main text.

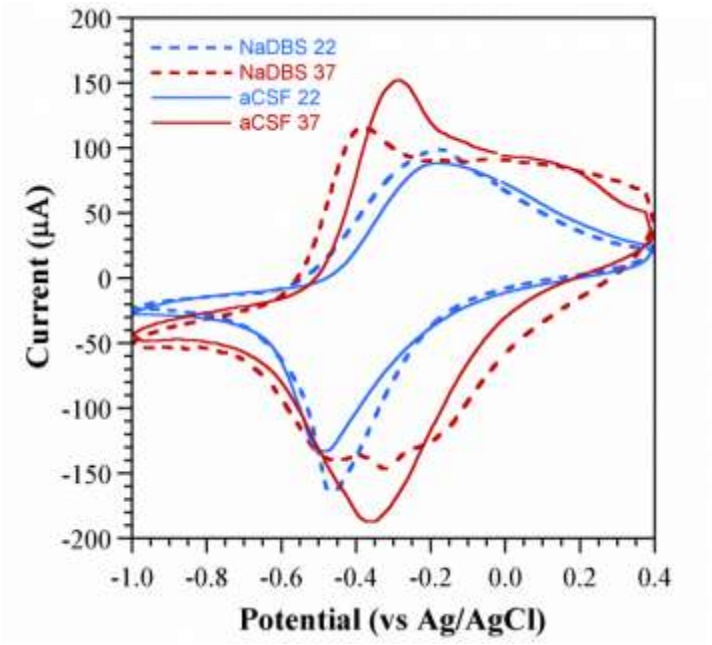

Sup. Figure 7. Typical cyclic voltammograms in the four solutions.

S4. Deflection upon voltage stepping

During slow potential scanning the deflection is limited by the scan rate, but under a voltage step the speed is determined by the rate-limiting oxidation or reduction process, typically mass transport of the solvated ions within the polymer [73]. To ascertain the speed of the actuators, voltage stepping was carried out. Three new samples were primed by performing ten CVs at 25 mV/s; two in NaDBS

at RT and one in aCSF at RT. Next, the samples were stepped ten times between 0.4 V and -1.0 V using a voltage square wave, holding each potential for 240 seconds. One was stepped in NaDBS at RT (NaDBS-NaDBS) and two in aCSF at 37 °C (NaDBS-aCSF & aCSF-aCSF). The tip deflections from the video and the current data were synchronized and segmented into reduction and oxidation partitions. The deflections from the final cycle are shown in Sup. Figure 8. Curve fitting was accomplished using Matlab, and rise and fall time constants were obtained.

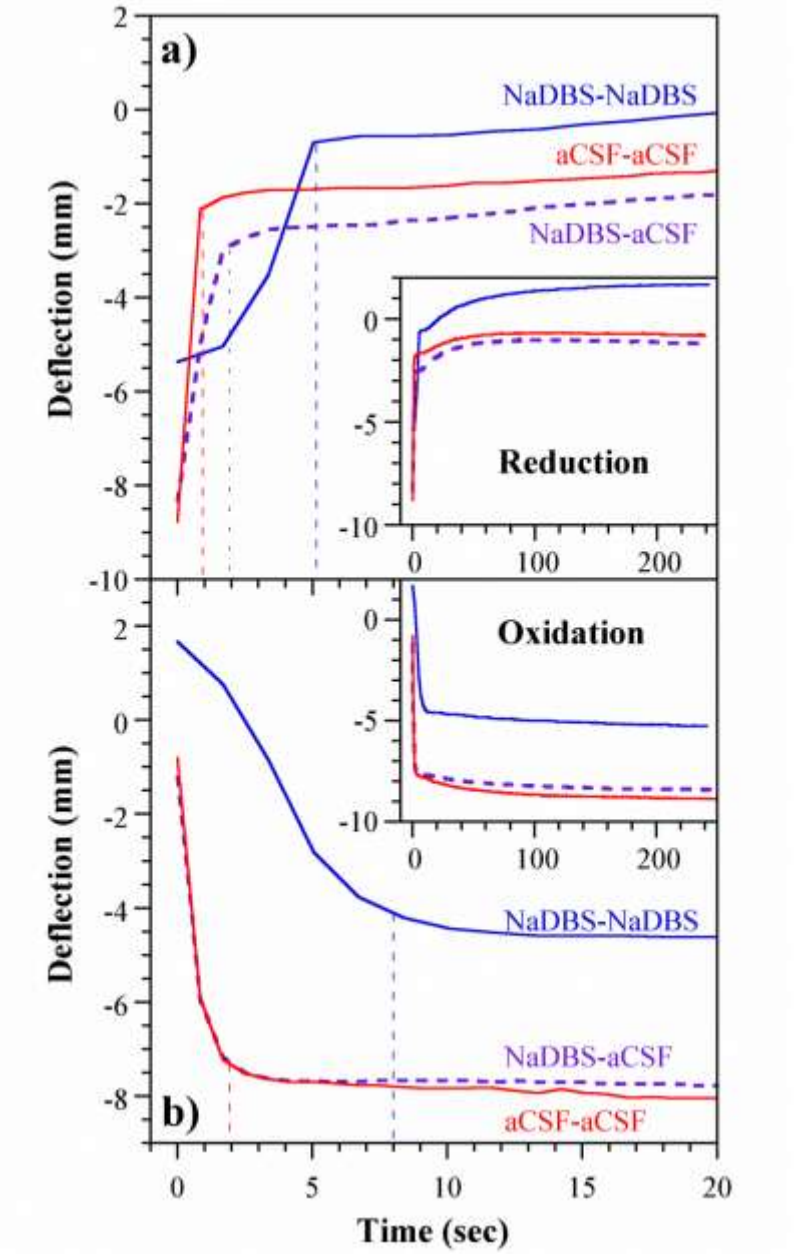

Sup. Figure 8. Preliminary data for 3 samples (one per group). Deflection during the 10th step between 0.4 V and –1.0 V either in NaDBS at RT or in aCSF at 37 °C after prior electrochemical cycling in one of these two solutions at RT. NaDBS-NaDBS indicates priming in NaDBS followed by stepping in NaDBS.

Tip deflections comprised an initial fast movement that took on the order of seconds (indicated by the dashed vertical lines) followed by a slower movement that took place on the order of hundreds of seconds (shown in the inset). The two bilayers that were stepped in 37 °C aCSF moved more quickly during the first few seconds than the one in 22 °C NaDBS. The fast component, which would be the one used in actual applications, was approximately 5 seconds for reduction and 8 seconds for oxidation in 22 °C NaDBS, while it was 1-2 seconds for reduction and 2 seconds for oxidation in 37 °C aCSF, about 4 times faster. The increase in speed with temperature is fortunate for applications in the body.

Over longer times, the deflections gradually increased somewhat further. This is in the opposite direction as observed for salt draining in PPy(DBS) [74], instead suggesting a continued slow uptake of mass during reduction and loss of mass during oxidation, indicating a very slow-moving species or slow polymer chain motions [75].

S5. Transient effects upon voltage stepping

The data in Sup. Figure 8 are for the 10^{th} step in the second electrolyte. All 10 tip deflections in each electrolyte are shown in Sup. Figure 9. With each step, the final deflections under all three conditions, during both oxidation and reduction, shifted downward on the y axis, from positive displacements toward (more) negative ones. The shifts were larger in aCSF at 37 °C than they were in NaDBS at RT. For the NaDBS-aCSF (Sup. Figure 9c) condition, there were noticeable overshoots during reduction in which the deflection changed direction. Interestingly, the overshoot peak was not present during the first reduction step; instead, it was maximal in the second step and persisted until the fifth. A small overshoot was also seen in the second step upon raising the temperature from 22 °C to 37 °C in aCSF.

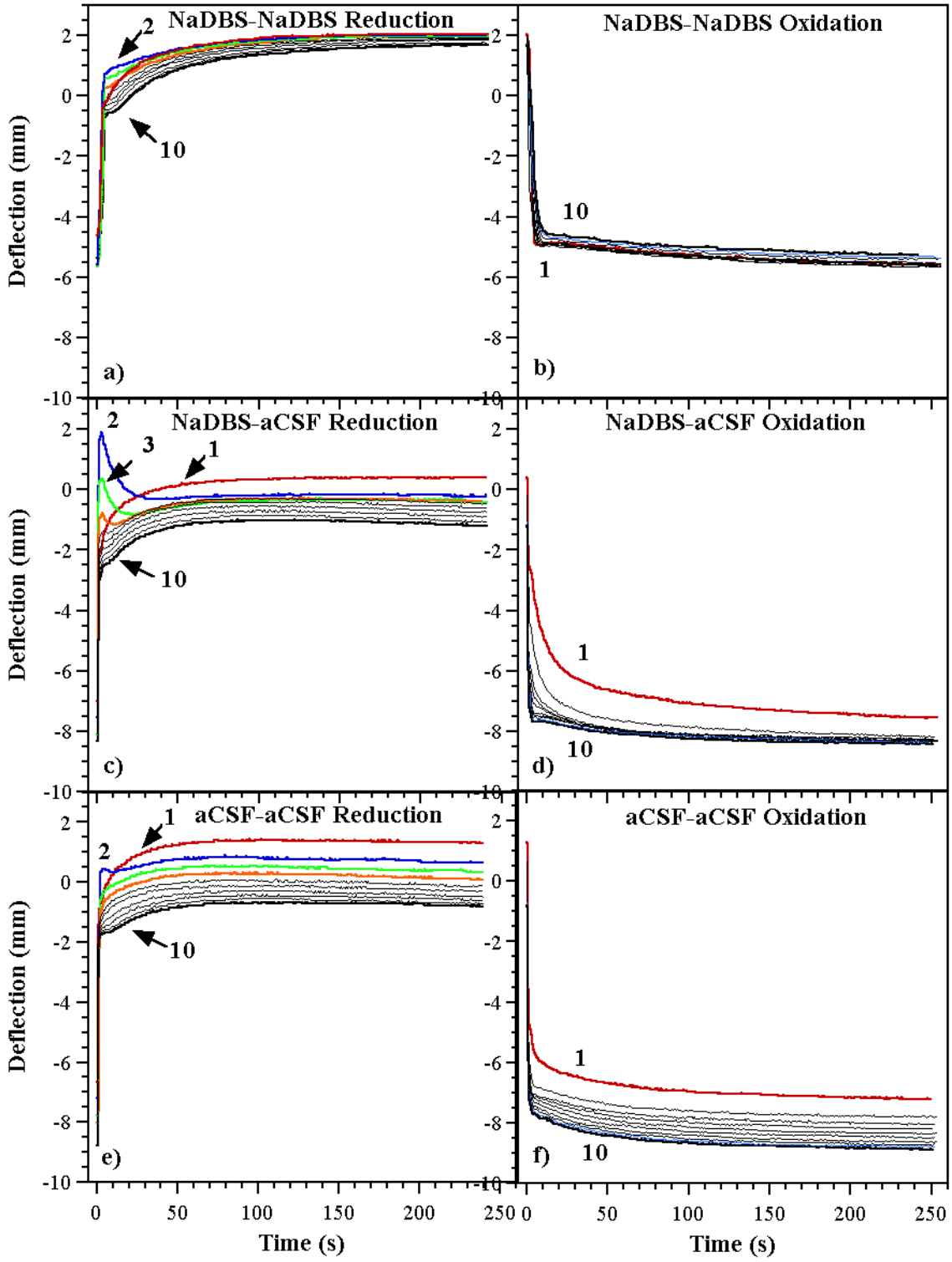

Sup. Figure 9. Preliminary data for 3 samples. Step responses of ten consecutive oxidation and reduction cycles, overlaid, in either NaDBS at RT or aCSF at 37 °C. Samples "NaDBS-aCSF" and "aCSF-aCSF" were stepped in 37 °C aCSF after priming in NaDBS at RT or aCSF at RT, respectively.

The transient deflection peaks during reduction of the NaDBS-aCSF sample were extracted from the deflection profile by subtracting scan 1 from subsequent scans and considering the "deflection overshoot" as the distance relative to scan 1's steady state value. The resultant peaks indicate the differences in the initial response and are shown in Sup. Figure 10. Despite the fact that the tip reached a steady final value, the overshoot peak reappeared in the next scan, although its magnitude decayed in each subsequent step. Even after ten scans there was a residual 0.8 mm overshoot that decayed over 5 sec. This transient peak was not found in the NaDBS-NaDBS sample, and it was less prominent in the aCSF sample primed in aCSF.

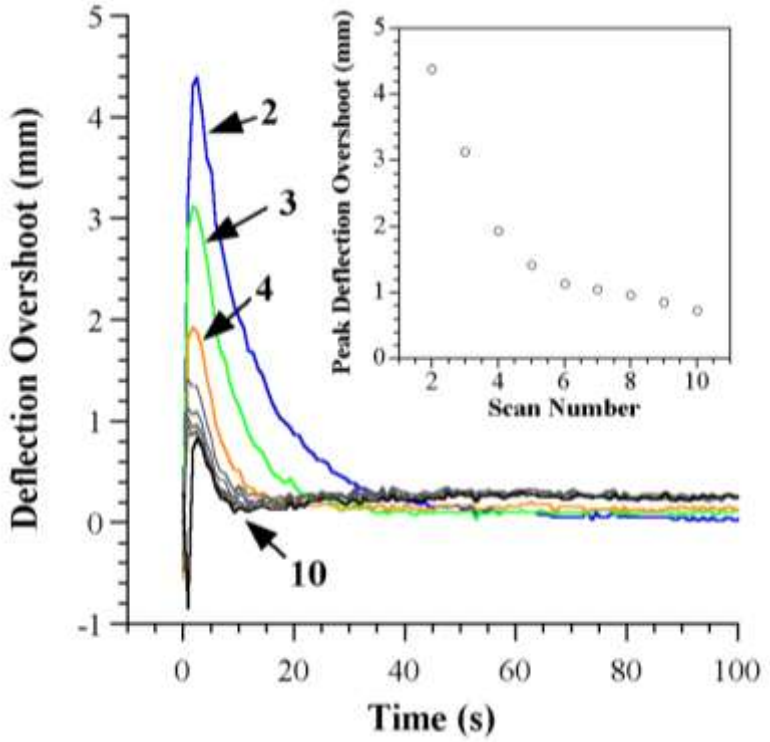

Sup. Figure 10. Preliminary data for 3 samples. Transient deflection peaks during reduction for scans 2-10 relative to scan 1 for the sample primed in NaDBS at RT and cycled in aCSF at 37 °C (NaDBS-aCSF, Sup. Figure 9c). Deflection overshoot is the difference of each scan relative to the steady state value of scan 1 (at 100 s). The peak deflection overshoots for scans 2-10 are plotted in the inset.

Reversals in beam motion have been seen when motion of one species in one direction is followed by motion of another species of the opposite charge in the opposite direction, with the time lag due to differences in mobility (and thus transport speeds) due to e.g. ion sizes [22, 40, 69, 76]. It is also known that the ions in conjugated polymers can be completely exchanged upon cycling in different electrolytes, and this was also shown for our PPy(DBS) system by the EDX spectra in **Error! Reference source not found.**. The reduction in the amplitude of the overshoot peak with cycle number is not inconsistent with replacement of the ions. Another interpretation is that the overshoot is related to water transport. Skaarup et al. reported an actuation-frequency-dependent strain and proposed that actuation speed depends not only on the transport rate of hydrated ions, but also on the

rate of movement of water that is not directly associated with ions due to changes in osmotic pressure as the ion concentrations within the polymer change [21]. The lesson from this transient behavior is that the actuators must be primed under the conditions in which they will be applied, or else ion-exchange phenomena may result in poor control during the initial cycles.

S6. Ramping voltage to attenuate initial transient effects

In section S5, the stepping experiments revealed a transient behavior. To further examine this, the applied voltage was ramped at different rates. Three fresh samples (polymerized together) were first primed by 10 CVs at 25 mV/s in either NaDBS at RT or aCSF at 37 °C. Immediately afterward (in the case of NaDBS-aCSF after transferring to the 2nd electrolyte), the actuators were held at +0.4 V for 100 seconds, ramped down to -1.0 V at 5 mV/s, and then held for 240 seconds. The priming-(transferring)-ramping procedure was repeated at voltage ramps of 50 and 500 mV/s in either NaDBS at RT or aCSF at 37 °C. The beam tip deflections are shown in Sup. Figure 11.

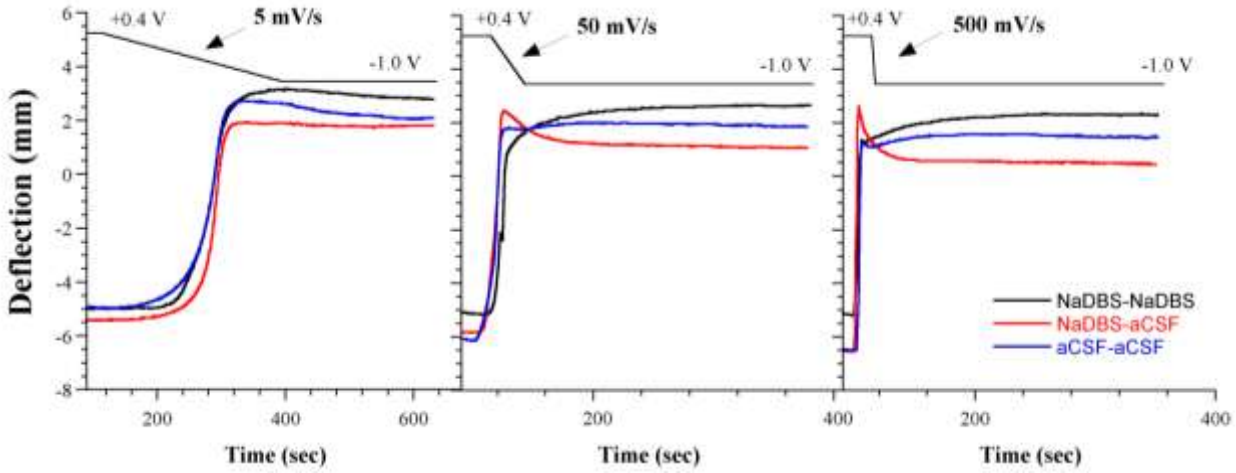

Sup. Figure 11. Deflection as a function of time in response to the voltage profiles shown at the top: samples were held at +0.4 V (oxidized) for 100 seconds, ramped to -1.0 V (reduced) at varying scan rates (5, 50, and 500 mV/s), and then held at -1.0 V for 240 seconds. Priming and ramping electrolytes were either NaDBS at RT or aCSF at 37 °C.

As expected, the bending behavior of the NaDBS-NaDBS sample was similar at the three ramp rates. However, the bending behavior of the NaDBS-aCSF sample depended strongly on the ramp rate, and that of the aCSF-aCSF sample less so.

At 5 mV/s, the deflections changed substantially monotonically, although the aCSF-aCSF sample drifted from its maximum deflection to a less curved state over the next 300 seconds, as did the NaDBS-NaDBS sample to a lesser extent. At 50 and 500 mV/s, the tip of the NaDBS-aCSF sample swung back again instead of remaining still. At 50 mV/s, the tip "overshot" by 1.3 mm beyond the final value (19% of the peak-to-peak value), reversed, and settled to its final position during the first 20 seconds. At 500 mV/s the overshoot was even larger at 2 mm (28% of the final value), but it settled to its final value in about half the time, within 11 sec.

These transients are likely due to multiple ion transport events with different rates, such as the incorporation of ions other than Na+ and the expulsion of Na+, although we cannot rule out contributions due to the expulsion of water or changes in chain conformation. As discussed in the previous section, transients are undesirable in an application setting. These results motivate future protocols for priming the actuators after deposition in an ionic medium and temperature matching those in the final application. A more thorough investigation would need to be performed to better understand the overshoot phenomenon.

S7. Calculation of curvature and actuation strain from deflection measurements

The curvature of the beam was obtained by trigonometry from the measured Δx and Δy deflections of the beam tip.

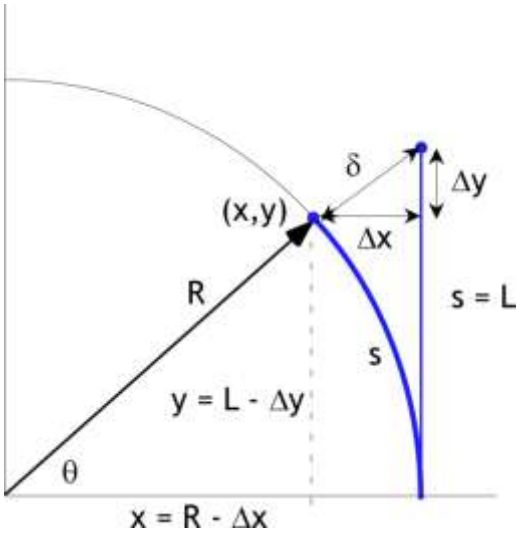

Sup. Figure 12. Trigonometry of beam bending used to obtain curvature.

(1) $$\delta = \sqrt{\Delta x^2 + \Delta y^2}$$

(2) $$R^2 = (L - \Delta y)^2 + (R - \Delta x)^2 = (L - \Delta y)^2 + R^2 - 2R\Delta x + \Delta x^2$$

(3) $$R = \frac{(L - \Delta y)^2 + \Delta x^2}{2\Delta x}$$

(4) $$\kappa = \frac{1}{R} = \frac{2\Delta x}{(L - \Delta y)^2 + \Delta x^2}$$

S8. Calculation of effective substrate modulus

The bilayer model

$$\kappa = \frac{\alpha_{PPy}}{h_{sub}} \frac{6mn(1+m)}{1+4mn+6m^2n+4m^3n+m^4n^2} \quad (5)$$

was used with an effective modulus E_{sub} for the Parylene+Cr+Au composite substrate. E_{sub} was determined by the transformed section method and the parallel-axis theorem to determine the moment of inertia for a composite area [54, 77]. In the transformed section method, the widths of the layers in the composite beam are adjusted to create an imaginary beam composed of only one material, in our case Au. The layer thicknesses for the Parylene, Cr, and Au were h_{Pa}, h_{Cr}, and h_{Au} respectively. (The beam width w cancels out).

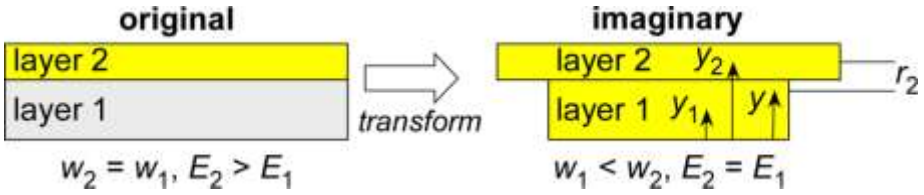

Sup. Figure 13. Beam cross-sections illustrating the transformed section method for a 2-layer beam.

The width ratios are given by n_i:

$$n_1 = \frac{E_{Cr}}{E_{Au}},\ n_2 = \frac{E_{Pa}}{E_{Au}}\ . \quad (6)$$

Next, the parallel-axis theorem is used to determine the moment of inertia for the imaginary beam. The moment of inertia I_{yi} of a layer with respect to the plane going through its center of mass is equal to the moment of inertia I'_{yi} with respect to any parallel plane plus the product of the area A_i and the square of the distance r_i between the two planes. The moment of inertia of a composite beam I_y is the sum of the moments of inertia of all the layers with respect to the same reference plane.

$$I_y = \sum_{i=1}^{n} I_{yi} = \sum_{i=1}^{n} I'_{yi} + A_i \cdot {r_i}^2 \quad (7)$$

where $r_i = y_i - y$ and y is the position of the reference plane. We choose to place the reference plane at the centroid (geometric center) of the imaginary beam, a distance y from the bottom of the beam, given by:

$$\mathrm{y} = \frac{\sum_{i=1}^{n} y_i A_i}{\sum_{i=1}^{n} A_i} = \frac{h_{Au}\left(h_{Cr}+h_{Pa}+\frac{h_{Au}}{2}\right)+ n_1 \cdot h_{Cr}\left(h_{Pa}+\frac{h_{Cr}}{2}\right)+ n_2 \cdot h_{Pa}\left(\frac{h_{Pa}}{2}\right)}{h_{Au} + n_1 \cdot h_{Cr} + n_2 \cdot h_{Pa}} \quad (8)$$

where y_i is the centroid of each layer and A_i is the cross-sectional area (thickness*width) of each transformed layer.

Substituting Equation (8) for every layer into equation y, I_y is given as:

$$(9) \qquad \mathrm{I}_y = w\begin{pmatrix} \frac{1}{12}{h_{Au}}^3 + h_{Au}\left(h_{Cr} + h_{Pa} + \frac{h_{Au}}{2} - \mathrm{y}\right)^2 + \frac{1}{12}n_1 \cdot {h_{Cr}}^3 \\ +n_1 \cdot h_{Cr}\left(h_{Pa} + \frac{h_{Cr}}{2} - \mathrm{y}\right)^2 + \frac{1}{12}n_2 \cdot {h_{Pa}}^3 + n_2 \cdot h_{Pa}\left(\mathrm{y} - \frac{h_{Pa}}{2}\right)^2 \end{pmatrix}$$

The composite substrate equivalent stiffness $(EI)_{sub}$ is obtained by multiplying the Young's modulus E of the reference layer, here E_{Au}, by $I_{y.}$

$$(10) \qquad (EI)_{sub} = E_{Au} \cdot I_y$$

The moment of inertia of the imaginary beam is I_{sub}.

$$(11) \qquad I_{sub} = \frac{1}{12}w \cdot (h_{Au} + h_{Cr} + h_{Pa})^3$$

E_{sub} is finally obtained by dividing the equivalent stiffness $(EI)_{sub}$ by I_{sub}.

$$(12) \qquad E_{sub} = \frac{(EI)_{sub}}{I_{sub}}$$

The Young's modulus E_{pa} for Parylene-C was reported by the manufacturer [78] to be 2.76 GPa, but another reports places it between 3.0-3.2 GPa [79] and a third as high as 4.75 GPa [80]. The manufacturer's value was used for this work. The bulk modulus for Au of E_{Au} = 83 GPa was used here, although the value for thin film gold has been reported as differing from this [33, 81]. The Cr adhesion layer is generally ignored, but it was thicker than usual on these beams (150 Å) and the Young's modulus E_{Cr} of Cr is high, ranging from 86 GPa up to 279 GPa in bulk Cr [82], so it may significantly contribute to the composite thickness. However, thin film deposited Cr has a reported value of 180 GPa [83]. Therefore, the conservative value of 180 GPa was used for this work. Using these values, the average E_{sub} was 5.07 ± 0.09 GPa. Strains derived from a multiple layer model [84] were compared with those from the bilayer model, and the difference was about 0.3%. The largest uncertainty was contributed by the Parylene layer thicknesses, which were known only to within ± 0.8 μm.

Sup. Table 2. Average actuation strain α, exchanged charge density, and strain-to-charge density (during reduction and oxidation and their sum) in the 9th and 19th scans under different cycling conditions, as well as the ratios of the 19th and 9th scan (n = 3).

Scan 9		NaDBS RT	NaDBS 37C	aCSF RT	aCSF 37C
α Reduction	%	0.46 ± 0.12	0.34 ± 0.02	0.43 ± 0.11	0.25 ± 0.00
α Oxidation	%	-0.35 ± 0.08	-0.46 ± 0.02	-0.23 ± 0.06	-0.39 ± 0.06
α Total	%	**0.81** ± 0.21	**0.80** ± 0.02	**0.66** ± 0.17	**0.64** ± 0.06
Re Charge Density	$C/m^3 \times 10^6$	101 ± 14	102 ± 19	89 ± 17	105*
Ox Charge Density	$C/m^3 \times 10^6$	82 ± 11	85 ± 8	69 ± 13	79*
Total Charge Density	$C/m^3 \times 10^6$	183 ± 24	187 ± 21	158 ± 28	184*
Re α/ Charge Density	$(\Delta l/l) / (C/m^3) \times 10^{-12}$	45.68 ± 13.89	33.24 ± 6.57	48.70 ± 15.35	23.35 ± 0.47
Ox α/ Charge Density	$(\Delta l/l) / (C/m^3) \times 10^{-12}$	-42.81 ± 11.47	-53.70 ± 5.76	-33.08 ± 10.88	-49.88 ± 7.66
Tot α/ Charge Density	$(\Delta l/l) / (C/m^3) \times 10^{-12}$	44.40 ± 12.64	42.54 ± 4.95	41.88 ± 13.08	34.74 ± 3.47

Scan 19		NaDBS RT	NaDBS 37C	aCSF RT	aCSF 37C
α Reduction	%	0.50 ± 0.14	0.20 ± 0.03	0.37 ± 0.11	0.10 ± 0.07
α Oxidation	%	-0.32 ± 0.13	-0.70 ± 0.07	-0.21 ± 0.04	-0.50 ± 0.04
α Total	%	**0.83** ± 0.25	**0.90** ± 0.07	**0.59** ± 0.15	**0.60** ± 0.11
Re Charge Density	$C/m^3 \times 10^6$	112 ± 9	182 ± 26	91 ± 4	176*
Ox Charge Density	$C/m^3 \times 10^6$	87 ± 13	133 ± 18	70 ± 2	135*
Total Charge Density	$C/m^3 \times 10^6$	199 ± 21	311 ± 44	161 ± 22	312*
Re α/ Charge Density	$(\Delta l/l) / (C/m^3) \times 10^{-12}$	45.03 ± 13.36	10.84 ± 2.10	41.08 ± 12.08	5.56 ± 3.86
Ox α/ Charge Density	$(\Delta l/l) / (C/m^3) \times 10^{-12}$	-37.34 ± 15.60	-52.61 ± 9.05	-30.47 ± 5.67	-37.26 ± 3.21
Tot α/ Charge Density	$(\Delta l/l) / (C/m^3) \times 10^{-12}$	41.67 ± 13.43	28.84 ± 4.59	36.47 ± 10.45	19.26 ± 3.49

Ratio of Scans 19/9	NaDBS RT	NaDBS 37C	aCSF RT	aCSF 37C
α Reduction	1.09 ± 0.43	0.58 ± 0.09	0.86 ± 0.33	0.40 ± 0.28
α Oxidation	0.93 ± 0.42	1.53 ± 0.18	0.93 ± 0.31	1.28 ± 0.22
α Total	**1.02** ± 0.40	**1.13** ± 0.09	**0.89** ± 0.32	**0.94** ± 0.19
Re Charge Density	1.11 ± 0.18	1.78 ± 0.42	1.02 ± 0.20	1.68*
Ox Charge Density	1.06 ± 0.21	1.56 ± 0.26	1.01 ± 0.19	1.71*
Total Charge Density	**1.09** ± 0.18	**1.66** ± 0.30	**1.02** ± 0.23	**1.70***
Re α/ Charge Density	0.99 ± 0.42	0.33 ± 0.09	0.84 ± 0.36	0.24 ± 0.17
Ox α/ Charge Density	0.87 ± 0.43	0.98 ± 0.20	0.92 ± 0.35	0.75 ± 0.13
Tot α/ Charge Density	**0.94** ± 0.40	**0.68** ± 0.13	**0.87** ± 0.37	**0.55** ± 0.11

* Denotes data from one sample.

S9. Cross-sectional images of devices showing delamination

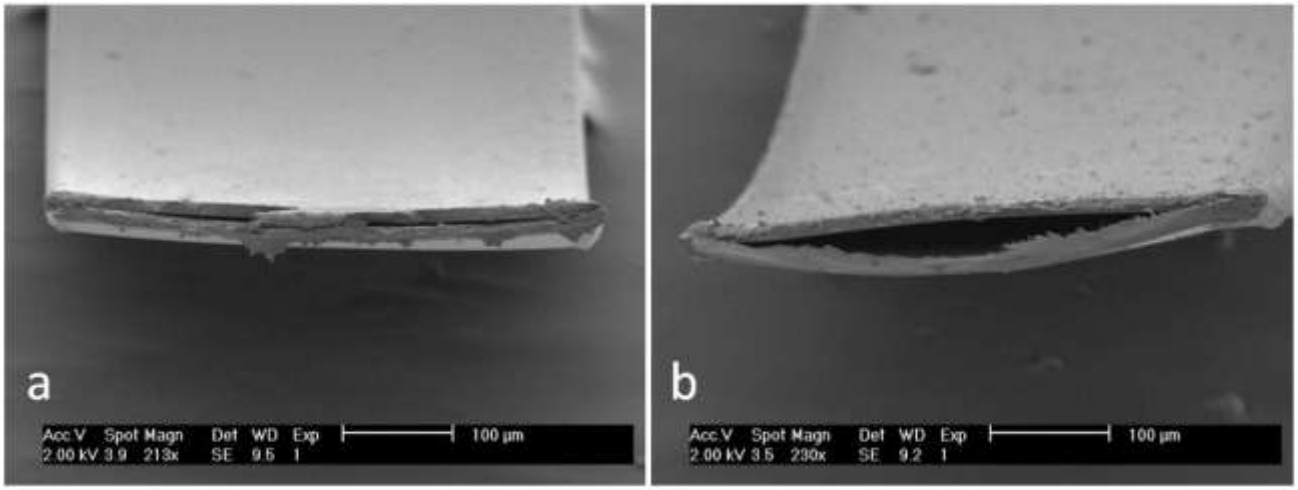

Sup. Figure 14. SEM images of bilayer cross sections of devices after being cut mid-length with some samples showing (a) no delamination and (b) delamination of the PPy layer. The delamination may have occurred during actuation or due to cutting.

In order to quantify the layer thicknesses, devices were cut using a razor blade midway along the length of the beam. Images of the cross-section of many of the devices showed signs of delamination, such as in Sup. Figure 14b. Delamination during actuation may explain the shifts in repeated CV current peaks as seen in S3, however, it is difficult to distinguish when the separation occurred.